Growth, microstructure, and failure of crazes in glassy polymers

Jörg Rottler* and Mark O. Robbins
Department of Physics and Astronomy, The Johns Hopkins University,
3400 N. Charles Street, Baltimore, Maryland 21218
(Dated: October 29, 2018)

We report on an extensive study of craze formation in glassy polymers. Molecular dynamics simulations of a coarse-grained bead-spring model were employed to investigate the molecular level processes during craze nucleation, widening, and breakdown for a wide range of temperature, polymer chain length N, entanglement length N_e and strength of adhesive interactions between polymer chains. Craze widening proceeds via a fibril-drawing process at constant drawing stress. The extension ratio is determined by the entanglement length, and the characteristic length of stretched chain segments in the polymer craze is $N_e/3$. In the craze, tension is mostly carried by the covalent backbone bonds, and the force distribution develops an exponential tail at large tensile forces. The failure mode of crazes changes from disentanglement to scission for $N/N_e \sim 10$, and breakdown through scission is governed by large stress fluctuations. The simulations also reveal inconsistencies with previous theoretical models of craze widening that were based on continuum level hydrodynamics.

PACS numbers: PACS: 81.05.Lg, 62.20.Fe, 83.10.Rs

I. INTRODUCTION

The failure of glassy polymers such as polystyrene (PS) or polymethylmethacrylate (PMMA) under external stresses occurs either through shear deformation or through crazing [1, 2]. While shear yielding occurs essentially at constant volume, crazing has a strong dilational component, and the volume of the material increases to several times its original value before catastrophic fracture occurs. Crazing is a failure mechanism unique to entangled polymeric materials and usually precedes a crack tip (see Fig. 1). The fundamental and technological importance of crazes is that they are in part responsible for the large fracture energy G_c of polymer glasses [3, 4, 5, 6] that makes them useful load-bearing materials. They control the crack tip advance and require a large amount of energy dissipation up to the point of catastrophic failure. Crazes can reach several μm in width and consist of an intriguing network of fibrils and voids that spans the entire deformed region.

Despite the frequent appearance of crazes, there is still comparatively little theoretical understanding about the conditions and mechanisms of craze nucleation, growth and ultimate breakdown [1, 2, 3, 4, 7, 15]. In this paper, we present an extensive set of nonequilibrium molecular dynamics (MD) simulations that address these various phenomena. In this approach, polymers are modeled on a coarse-grained scale that takes into account van-der-Waals (vdW) and covalent interactions without specific reference to chemical detail. The effect of chain length, temperature T, widening velocity v and vdW interaction strength on the craze structure can be studied over a wide range of parameters. The molecular simulations allow insight into microscopic details not accessible to
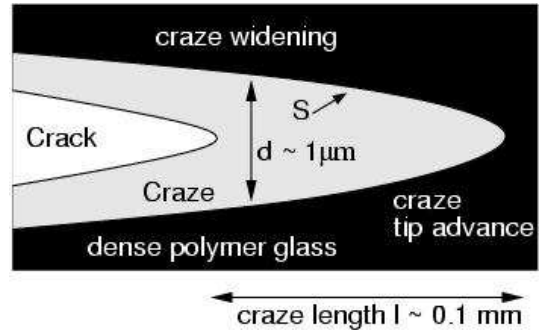
*Electronic address: rottler@pha.jhu.edu

FIG. 1: Craze fracture of glassy polymers. The craze is a deformed region (shaded) that grows in width and length under an applied vertical stress S. Its density is reduced with respect to the undeformed polymer by a constant extension ratio λ. Characteristic values for width d and length l are indicated. During growth, S acts perpendicular to the sharp interface between undeformed polymer and craze. Also shown is an advancing crack tip from the left that breaks the craze. Small representative volumes of each region are studied with molecular simulations.

experiments and offer an opportunity to test and develop theoretical models of crazing.

A fundamental limitation on molecular level treatments is of course the finite system size. The largest volumes accessible at present are $\sim 100 nm^3$, while the craze spans many μm. We are thus limited to a study of craze widening in a small representative region and cannot include e.g. the entire crack tip. Craze tip advance processes [15] are beyond the scope of the present work.

Several aspects of craze physics have already been adressed with simulations in previous papers. Baljon and Robbins [8, 9] demonstrated the importance of chain length for the onset of craze growth. Rottler *et al.* studied the elastic properties and fracture stresses of fully evolved crazes and used them in combination with linear

fracture mechanics to calculate the macroscopic fracture energy of glassy polymers that fail by crazing [6]. Rottler and Robbins also investigated how polymer entanglements affect the craze structure on a microscopic level and argued that they "jam" the expansion of the glass under tension [10].

This paper extends the previous work and is organized as follows. In Section II, we briefly summarize the key experimental observations and review existing theoretical models of crazing. Section III gives the technical details of the molecular models used in this study. We then analyze results for craze nucleation (Section IV), growth (Section V), microstructure (Section VI), and failure (Section VII), and compare our findings to previous models and experiments. Final conclusions are offered in Section VIII.

II. CRAZE PHENOMENOLOGY AND THEORY

A. Experiments

Crazes have been studied experimentally for more than 30 years [11, 12, 13, 14, 15]. The techniques most commonly used to analyse the craze structure are transmission electron microscopy (TEM) [17, 18], low angle electron diffraction (LAED) and small angle x-ray scattering (SAXS) [19, 20, 21]. Comprehensive reviews of theoretical and experimental results have been presented by Kramer and Berger [14, 15] and Creton *et al.* [16].

The density in the undeformed polymer ρ_i and craze ρ_f is obtained from TEM measurements. The increase in volume during craze formation, or extension ratio $\lambda \equiv \rho_i/\rho_f$, is found to have a characteristic value for a given polymer that is independent of molecular weight. Typical values of λ for different polymers range from two to seven.

Real space images of the craze show that the polymers are bundled into fibrils that merge and split to form an intricate network. The fibrils are highly aligned with the applied tensile stress and vary in diameter and length. However, this complex structure is normally idealized as a set of uniform vertical cylinders connected by short cross-tie fibrils [15]. The characteristic fibril diameter $\langle D \rangle$ and separation $\langle D_0 \rangle$ (see Fig. 2) are then determined from a Porod analysis of scattering experiments (see Section V). Measured values range between $3 - 30$ nm for $\langle D \rangle$ and $20-50$ nm for $\langle D_0 \rangle$ [14, 15, 22, 23]. For example, for polystyrene one obtains $\langle D \rangle \sim 6$nm and $\langle D_0 \rangle \sim 20$nm [1].

Nucleation of crazes [12] occurs preferentially near defects in the polymer. These produce large local tensile stresses that lead to the formation of microvoids that evolve into a craze. Once nucleated, the craze grows in length and width (see Fig. 1). It is well established [15] that the craze widens by drawing material from the dense polymer into new fibrils. This deformation is confined to a narrow active zone at the interface between the dense polymer and craze. The width of the active zone h (see also Fig. 2) is usually between $\langle D \rangle$ and $\langle D_0 \rangle$. Craze widening is a steady-state process, in which a constant "drawing stress" S ranging between 20 and 100MPa is applied. Typical experimental values are 35 MPa (polystyrene) [14] and 70 MPa (polymethymethacrylate) [38]. The value of S is of the same order as the shear yield stress of the polymer, and is found to increase with the entanglement density.

B. Theory

A theory of crazing has to explain the molecular origin of the craze structure and the interdependencies of the various quantities measured in experiments. Despite a wealth of experimental data on crazing, there is currently no theoretical description that addresses all aspects of craze physics. The following models have been proposed to explain the extension ratio λ and the relationship between fibril spacing $\langle D_0 \rangle$ and drawing stress S.

1. The extension ratio λ

The extension ratio λ has been successfully explained by a simple scaling argument, that relates λ to the microscopic entanglement network in the polymer glass. Entanglements arise in dense polymeric systems from the topological constraints that the chains impose upon each other. The mobility of the chains is greatly restricted, because they cannot pass through each other. The starting point for the present argument is the assumption that the glass inherits these entanglements from the melt, where an entanglement molecular weight is given by the plateau modulus under shear, $G_N^{(0)}$:

$$M_e = \rho 4RT/5G_N^{(0)}. \tag{1}$$

This result can be derived from the microscopic tube model [24], which relates the rheological response of the polymer melt to the deformation of a tube to which the polymer chain is confined. With repeat units of weight M_0, one can define a typical number of steps $N_e = M_e/M_0$ (entanglement length) between entanglements along the polymer backbone.

These entanglements are assumed to act like permanent chemical crosslinks during crazing, which implies that the expansion ends when segments of length N_e are fully stretched. The initial separation of entanglement points is $d_i = (l_p l_0 N_e)^{1/2}$, according to standard random walk (RW) scaling, where l_0 is an elementary step length and l_p the persistence length. The length of this segment rises from d_i to a maximum final length $d_f = \lambda_{\max} d_i = N_e l_0$, and thus

$$\lambda_{\max} = (N_e l_0/l_p)^{1/2}. \tag{2}$$

Experimentally, Eq. (2) is well confirmed, but Section V D shows that the picture motivating this expression is oversimplified.

2. The drawing stress S

The value of the drawing stress S has traditionally been related to the craze microstructure ($\langle D \rangle$, $\langle D_0 \rangle$) via capillary models [14, 15]. In these models, the polymer in the active zone is treated as a viscous fluid with a surface tension Γ and a viscosity η. Figure 2 shows an idealized picture of the craze geometry, where craze formation is modelled as the propagation of void fingers with a characteristic spacing $\langle D_0 \rangle$ into the strain-softened fluid. The applied stress S required to advance the interface has a dissipative contribution arising from a suitable flow law (e.g. power-law fluid) and an energy penalty contribution due to the surface tension. The tension is S in the polymer glass and the Laplace pressure $2\Gamma/(\langle D_0 \rangle/2)$ at the ceiling of the finger, where $\langle D_0 \rangle/2$ is the characteristic radius of curvature (see Fig. 2). By estimating the width of the active zone as $h \sim \langle D_0 \rangle/2$, Kramer calculated a stress gradient between glassy polymer and the finger void ceiling,

$$\nabla\sigma \sim \frac{\Delta\sigma}{h} \sim \frac{S - 4\Gamma/\langle D_0 \rangle}{\langle D_0 \rangle/2}. \tag{3}$$

Since $\nabla\sigma$ is proportional to the interface velocity, he then predicted that the system will select a value of

$$\langle D_0 \rangle \sim 8\Gamma/S, \tag{4}$$

which maximizes the stress gradient between finger ceiling and bulk polymer and thus will lead to the fastest propagation velocity of the fingers.

More recently, Krupenkin and Fredrickson [7] have formulated a theory of craze widening that is similar in spirit to Kramer's arguments and also equates the craze widening stress with a viscous and a surface tension contribution. However, these authors suggest a different interpretation of Γ. They introduce an effective surface tension that begins to rise above the vdW value when the finger radius rises above the rms spacing between entanglement lengths d_i. This ansatz is motivated by the idea that expanding the random walk between entanglements generates an additional energy penalty. An upper bound to Γ is provided by the energy required for chain breaking, which sets in once the finger radius exceeds the maximum elongation between entanglement points, $l_0 N_e$. By minimizing the finger propagation stress, they conclude that the fibril spacing will always be

$$D_0 \sim d_i, \tag{5}$$

independent of surface tension. In their model, the fibril spacing is determined exclusively by the entanglement network.
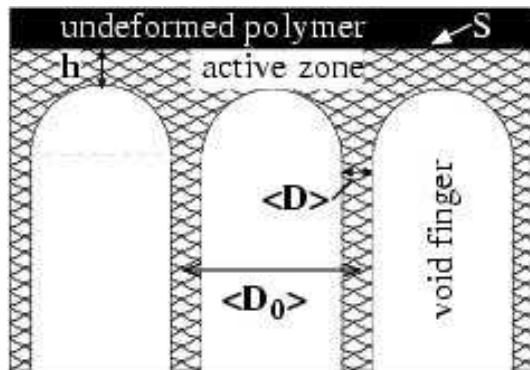

FIG. 2: Surface tension model of craze widening. Void fingers with characteristic spacing $\langle D_0 \rangle$ propagate into a strain-softened layer of polymer fluid of width h, leaving behind fibrils of a characteristic diameter $\langle D \rangle$. The externally applied stress S acts perpendicular to the fluid-glass interface. The characteristic radius of the finger caps is on the order of $\langle D_0 \rangle/2$. (See Refs. [14, 15] for an analogous figure.)

III. SIMULATIONS AND MOLECULAR MODELS

We study craze formation by performing molecular dynamics simulations of a standard coarse-grained polymer model [25], where each linear polymer contains N spherical beads of mass m. Models of this kind have a long tradition in polymer research and have verified theories of polymer dynamics [24] in the melt. They have recently been employed by other researchers to study failure in network polymer adhesives [27] and end-grafted polymer chains between surfaces [28].

In this bead-spring model, van der Waals interactions between beads separated by a distance r are modeled with a truncated Lennard-Jones potential:

$$V_{LJ}(r) = 4u_0 \left[(a/r)^{12} - (a/r)^6 - (a/r_c)^{12} + (a/r_c)^6 \right] \tag{6}$$

for $r \leq r_c$, where $u_0 \sim 20 - 40$ meV and $a \sim 0.8 - 1.5$ nm are characteristic energy and length scales [26]. A simple analytic potential [28]

$$V_{br}(r) = -k_1(r - R_0)^3(r - R_1) \tag{7}$$

is used for covalent bonds between adjacent beads along the chain. The form of this potential was chosen to allow for covalent bond breaking, which is not possible with other standard bond potentials such as the popular FENE potential [25]. Bonds are permanently broken when r exceeds $R_0 = 1.5\,a$. The constant $R_1 = 0.7575a$ was chosen to set the equilibrium bond length $l_0 = 0.96\,a$, which is the "canonical" value for the bead-spring model with the FENE potential [25]. This allows us to use results from previous studies, most importantly the entanglement length. The constant k_1 determines the ratio of the forces at which covalent and van der Waals bonds break. We find that this ratio is the only important parameter in the covalent potential and set it to 100

based on data for real polymers [27, 28], which implies $k_1 = 2351u_0/a^4$. Tests with other analytical forms of the bond potential showed no appreciable impact on our results as long as the bonds break before the chains can pass through each other.

In order to vary the entanglement length, we include a bond-bending potential [28, 29]

$$V_B = b \sum_{i=2}^{N-1} \left(1 - \frac{(\vec{r}_{i-1} - \vec{r}_i) \cdot (\vec{r}_i - \vec{r}_{i+1})}{|(\vec{r}_{i-1} - \vec{r}_i)||(\vec{r}_i - \vec{r}_{i+1})|} \right) \quad (8)$$

that stiffens the chain locally and increases the radius of gyration. Here, $\vec{r}_i$ denotes the position of the ith bead along the chain, and b characterizes the stiffness. We will consider two cases here referred to as flexible ($b = 0$) and semiflexible ($b = 1.5u_0$) polymers. The corresponding entanglement lengths are $N_e^{\text{fl}} \approx 70$ and $N_e^{\text{sfl}} \approx 30$ beads, respectively [25, 26, 29].

We consider three temperatures $T = 0.01\, u_0/k_B$, $T = 0.1\, u_0/k_B$ and $T = 0.3\, u_0/k_B$, where the last temperature is close to the glass transition temperature. The amount of adhesive interaction between beads is varied by changing the range r_c of the LJ potential from $1.5a$ to $2.2a$.

The equations of motion are solved using the velocity Verlet algorithm with a timestep of $dt = 0.0075\, \tau_{\text{LJ}}$, where $\tau_{\text{LJ}} = \sqrt{ma^2/u_0}$ is the characteristic time given by the LJ energy and length scales. Periodic boundary conditions are employed in all directions to eliminate edge effects. The temperature is controlled with a Nosé-Hoover thermostat (thermostat rate $1\,\tau_{\text{LJ}}^{-1}$), and the thermostat is only employed perpendicular to the direction of craze growth. Simulations with a Langevin thermostat showed no appreciable difference between the two methods.

In all simulations of crazing, an initial isotropic state in a cubic simulation cell of edge length L is created using standard techniques [26]. Polymer chains are constructed as ideal RWs with a suitably chosen persistence length l_p. l_p is fixed by matching the radius of gyration of the chains to the equilibrium value in the melt, and the values are $l_p^{\text{fl}} = 1.65a$ and $l_p^{\text{sfl}} = 2.7a$ for flexible and semiflexible chains, respectively. Subsequently, the interaction potentials are imposed and the system is cooled at constant volume from a melt temperature $T_m = 1.3u_0/k_B$, to the desired run temperature.

All runs begin at zero hydrostatic pressure. Strains ϵ_{ii} are then imposed by rescaling the simulation box periods L_i and all particle coordinates proportionally [30]. This allows arbitrary stress states to be studied in Section IV.

IV.   CRITERIA FOR CAVITATION AND CRAZE NUCLEATION

The loading conditions on the polymer glass determine whether it will fail initially by shear yielding or the formation of voids and cavities. In general, strong triaxial
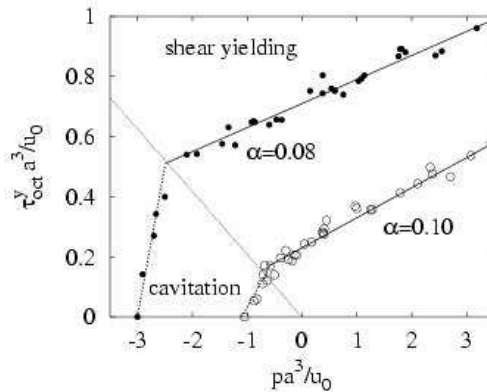

FIG. 3: Octahedral shear stress τ_{oct}^y at yield as a function of pressure p at two different temperatures $T = 0.3u_0/k_B$ (open symbols) and $T = 0.01u_0/k_B$ (filled symbols). The solid lines are fits to Eq. (9) and the dashed lines show the onset of cavitation. Values of α are indicated for the two temperatures. Also drawn is a dotted line through the transition points that separates the regions of shear and cavitational failure. Here yield is associated with the strain where τ_{oct} peaks.

tensile stresses will favor cavitation. Cavitation and crazing are closely related, because crazes usually require the initial formation of microvoids [15]. We therefore first address the initial failure of the polymer glass through either shear yielding or cavitation, and later discuss the formation of crazes.

The loading conditions that lead to shear yielding in many experimental polymers [31, 32] are most accurately represented by the pressure-modified von Mises yield criterion. It is formulated in terms of simple stress invariants, the hydrostatic pressure $p = -(\sigma_1 + \sigma_2 + \sigma_3)/3$ and the deviatoric or octahedral shear stress $\tau_{\text{oct}} = \left((\sigma_1 - \sigma_2)^2 + (\sigma_2 - \sigma_3)^2 + (\sigma_3 - \sigma_1)^2\right)^{1/2}/3$, where the σ_i denote the three principal stress components. The pressure-modified von Mises criterion states that yield will occur at an octahedral yield stress τ_{oct}^y given by

$$\tau_{oct}^y = \tau_0 + \alpha p, \quad (9)$$

where τ_0 is the yield stress at zero hydrostatic pressure and α is a dimensionless constant. Its physical motivation is that the elastic free energy stored in shear deformation is proportional to τ_{oct}^2 and failure should occur when this energy exceeds a threshold that rises slowly with p.

In ref. 33, we examined a much larger range of stress states than in previous experimental studies and showed that the pressure-modified von Mises criterion provides a good description of shear yield in our bead-spring model. Data for two extremal temperatures are replotted in Fig. 3 along with solid lines showing fits to Eq. (9). Shear yield was observed to the right of the dot-dashed line, and these data points follow Eq. (9) quite accurately. To the left of the line cavitation was observed. The deviation

from the von Mises fits is very sharp, and τ_{oct} quickly drops to zero. The values of τ_{oct}^c where cavitation occurs are well described by a straight lines

$$\tau_{oct}^c = \tau_0^c + \alpha^c p \tag{10}$$

with new constants τ_0^c and α^c. This new "cavitation criterion" can be motivated in analogy to the von Mises criterion by assuming that the elastic free energy F_V associated with volume changes must reach a critical value for cavitation to occur. F_V is proportional to p^2, which gives a criterion of the form $p = p_0$. One can then assume that shear components in the stress tensor aid cavitation in a linear fashion, i.e. $p = p_0 + \tau_{\text{oct}}/\alpha_c$, which can be rearranged to give Eq. (10) with $\tau_0^c = \alpha_c p_0$.

No clear experimental consensus exists about the stress state required for crazing, partly because of the importance of surface defects in nucleating crazes. However, several criteria for craze nucleation were proposed almost 30 years ago. They all try to take into account the critical role of tensile stress components. Sternstein *et al.* [35] suggested a craze yield criterion of the form

$$\tau_{\text{max}} \equiv \frac{1}{2}|\sigma_i - \sigma_j|_{\text{max}} = A + B/p, \tag{11}$$

where A and B are constants that depend on temperature. With respect to our criterion Eq. (10), p has been replaced by $1/p$ and τ_{oct} by the largest difference between any two stress components. Bowden and Oxborough [1] formulated a similar criterion, where τ_{max} is replaced by $\sigma_1 - \nu\sigma_2 - \nu\sigma_3$ and ν is Poisson's ratio for the polymer glass. This expression is another possibility to describe the shear components of the stress state, and it reduces to τ_{max} when $\nu = 1/2$ and $\sigma_2 = \sigma_3$. The Sternstein and Bowden and Oxborough expressions could in principle also be fitted to the rather narrow range of pressure in Fig. 3 where cavitation occurs. However, we are unaware of a convincing physical motivation for the $1/p$ term, which leads to obvious analytical problems at small p. In addition, the experimental results that motivated Eq. (11) are sensitive to surface defects [12].

The above considerations pertain to the *initial* mode of failure of the polymer glass at strains typically less than 10%. However, crazing is a large strain deformation with strains of several hundred percent. Although we find voiding to be a neccessary precursor to crazing, it is not guaranteed that a loading state that leads to cavitational failure according to Eq. (10) will ultimately produce stable crazes. Likewise, we have observed that an initial failure through shear deformation can still lead to later void formation and crazing. One should thus strictly call Eq. (10) a cavitation failure criterion and not a craze yielding criterion.

V. GROWTH OF CRAZES

In order to induce crazing, we enforce cavitation by expanding the periodic simulation box in the z-direction at constant velocity while maintaining the simulation box periods in the perpendicular $x - y$ plane. This leads to an initial stress state where all three principal stresses are tensile. The initial voids formed during cavitation expand upon further straining, but their growth rapidly becomes arrested [9]. Instead of forming new voids, additional material is drawn out of the uncavitated polymer, and stable craze growth occurs. In our simulations, growth continues until all material in the simulation box is converted into the craze.

A. Images of crazes

A good impression of the crazing process can be obtained by inspecting the snapshots of the simulation cell shown in Figs. 4 - 6. Each slice has a lateral width of $64\,a$, and three different strains are shown. In all images, the chain length $N = 512$. Previous studies [9] had shown that N has to be twice the entanglement length or greater in order to form stable crazes. For shorter chains, the material cavitates, but then rapidly fails due to chain pullout. In the following, we only consider chains with $N \geq 2N_e$.

Note first that in all cases, there is a sharp interface between dense polymer and crazed material. This narrow 'active zone' is one of the key features of craze phenomenology found in experiment. In the craze, the polymer chains have merged into fibrils that are strongly aligned. However, the structure is quite complicated, as there are many lateral connections between fibers.

One can also observe that the fine structure of the crazes in the three sequences varies greatly. Fig. 4 with flexible chains at the low temperature of $T = 0.1u_0/k_B$ and the weak adhesive interaction (cutoff distance $r_c = 1.5a$) shows many thin fibrils, whereas the fibrils in Fig. 6 at the higher temperature of $T = 0.3u_0/k_B$ and the stronger adhesive interaction $r_c = 2.2a$ are much thicker in diameter. These trends are not surprising, because increased chain mobility at higher temperatures and stronger adhesive interactions should drive the system to larger fibril diameters, which minimize the surface area.

B. The drawing process and stress-strain curves

A second characteristic feature of craze growth is that deformation occurs at a constant plateau or drawing stress S. This plateau can be easily identified in the stress-strain curves shown in Fig. 7. The curves can be separated into three different regimes. In regime I, the stress rises to a peak of $\sim 2.6u_0/a^3$ and then drops when the polymer yields by cavitation. Following cavitation, the stress rapidly relaxes and remains at the plateau value S in regime II, the growth regime. Regime II is much shorter in the semiflexible case Fig. 7(b) than in the flexible case Fig. 7(a) (note different lateral scales).
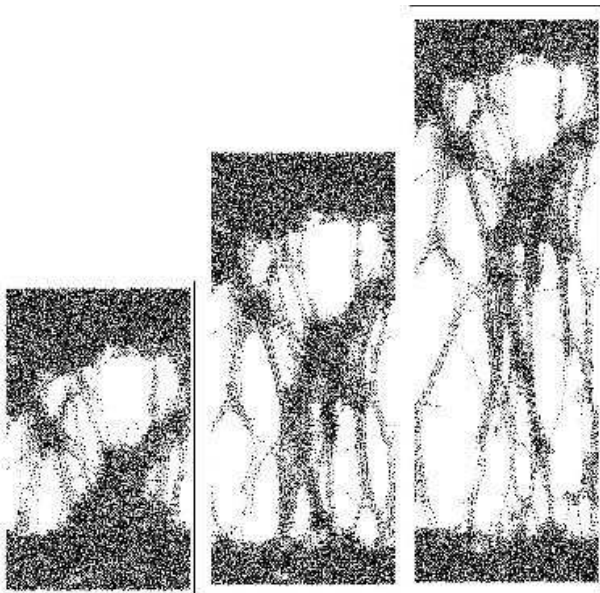
FIG. 4: Three snapshots of craze growth for flexible chains with $T = 0.1u_0/k_B$ and $r_c = 1.5a$. The total system contains 262144 beads, but only slices of thickness $10a$ normal to the page are shown in order to resolve the fine structure. The lateral dimension of each slice is $64a$ and the vertical direction is to scale. Each dot represents one Lennard-Jones bead.
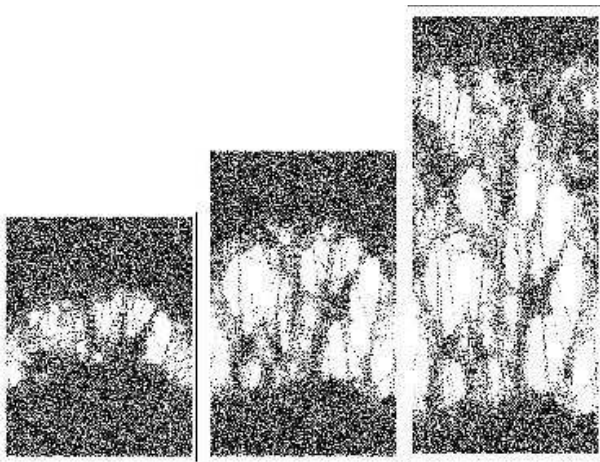

FIG. 5: Three snapshots of craze growth for semiflexible chains with $T = 0.1\,u_0/k_B$, $r_c = 1.5\,a$, and 262144 beads.

Regime II ends when the strain L_z/L reaches the extension ratio λ. At this point, all the material in the simulation cell has been converted into the craze, and additional deformation strains the entire craze uniformly. As a consequence, the stress rises again in regime III. This regime finally ends in catastrophic failure either through chain disentanglement or chain scission (see Section VII).

Note first that neither the peak stress at cavitation nor the value of S depends on the chain length N. The curves for different N in Fig. 7 only split apart after
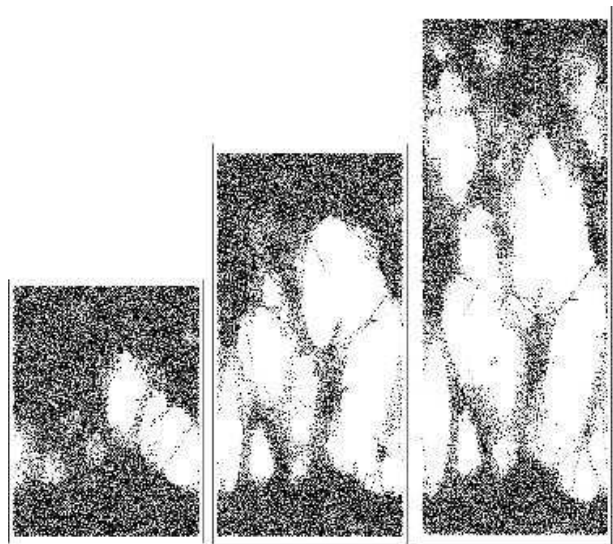

FIG. 6: Three snapshots of craze growth for semiflexible chains with $T = 0.3\,u_0/k_B$, $r_c = 2.2\,a$, and 262144 beads.

completion of craze growth when L_z/L reaches λ and the entire craze is strained. Baljon and Robbins [9] showed that the peak stress remained constant for much shorter chains, but that regime II only appeared when N was $2N_e$ or longer. Another important fact to note is that S is independent of system size. For example, values of S in systems ranging between 32768 and 1048576 beads are the same within a few percent. The biggest change with increasing system size is that temporal fluctuations in S decrease.

In Fig. 8(a), we analyze trends of S with T and r_c. The drawing stress decreases linearly with increasing temperature and increases with increasing adhesive interactions (i.e. increasing r_c). Fig. 8 (b) shows that S varies logarithmically with the widening velocity v over two orders of magnitude, which is indicative of a thermally activated process. For the subsequent figures, we choose $v = 0.06a/\tau_{\text{LJ}}$, which is at the upper end of the logarithmic regime [9]. Similar behavior is also found for the shear yield stress of glassy polymers [33, 34].

C. Crazing under plane stress conditions

The results of Section IV show that cavitation only occurs when all three principal stresses are tensile. Many experimental crazes grow in a thin film geometry under plane stress conditions. However, in these experiments the craze is often prenucleated or nucleates near a defect [12]. This situation can also be mimicked in our simulations. To this end, the periodic boundary conditions in the x direction were replaced with free boundaries, so that the solid is free to relax in that direction. Initial failure is now nucleated by placing 1000 purely repulsive LJ beads in the center plane of the simulation cell located
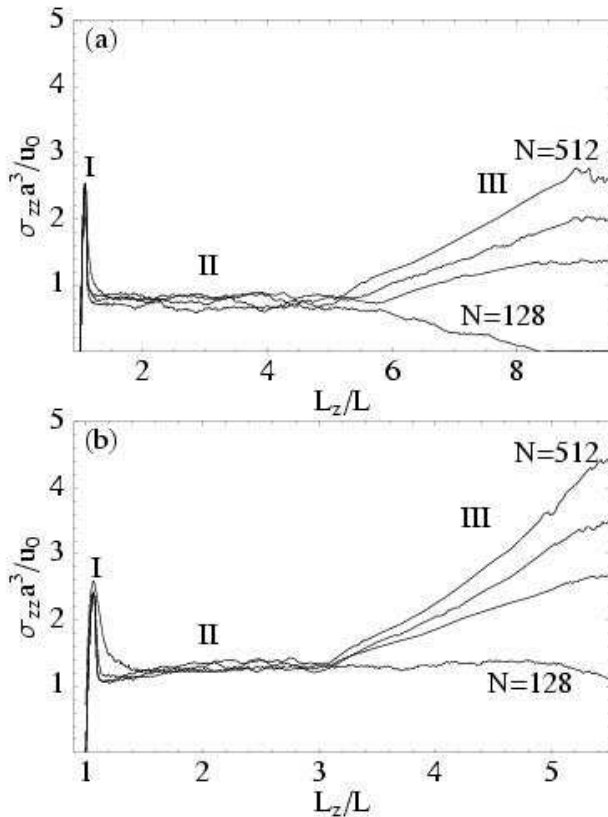
FIG. 7: Stress σ_{zz} in the widening direction during craze growth at $T = 0.1\,u_0/k_B$, $r_c = 1.5a$ for (a) flexible and (b) semiflexible chains of length $N = 128$, $N = 256$, $N = 384$, and $N = 512$. Three characteristic regimes of (I) cavity nucleation, (II) craze growth and (III) craze failure are also indicated. The two perpendicular stress components σ_{xx} and σ_{yy} also peak at cavitation (see text), but then rapidly drop to zero. Qualitatively identical curves are obtained at other values of T and r_c.

at $z = L_z/2$ [42]. This weakens the solid locally and constrains the location of initial failure, while not affecting subsequent craze growth.

Fig. 9 shows three snapshots of a craze in this geometry. As in experiments, necking is observed at the craze-bulk interface. Although σ_{xx} vanishes in the rest of the film, the neck produces strong tensile stresses in all three directions in the active zone. The craze grows in the same fashion as in the simulations with 3D periodic boundary conditions. Since the latter yield better statistics for the craze structure, we have focused on this methodology for our analysis.

D. The extension ratio

The extension ratio λ can be calculated from the average densities of crazed and uncrazed material. Fig. 10 shows how the density drops from the initial value ρ_i to
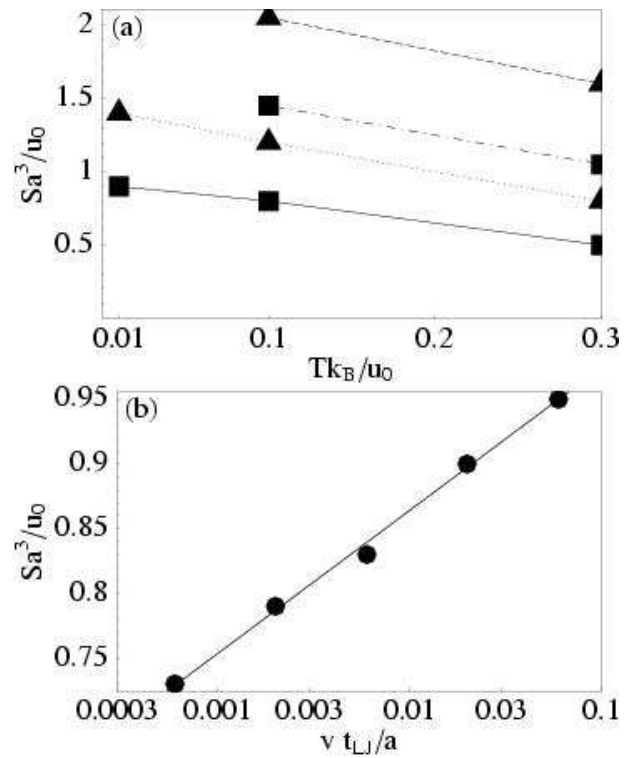

FIG. 8: (a) Trends of S with T and r_c at $v = 0.06a/\tau_{LJ}$ for flexible ($\blacksquare$) and semiflexible ($\blacktriangle$) chains and $r_c = 1.5a$ (lower curves) and $r_c = 2.2a$ (upper curves). (b) Velocity dependence of S for flexible chains at $T = 0.1u_0/k_B$. The straight line is a fit to a logarithmic velocity dependence, $S = 1.085\,u_0/k_B + 0.048\,u_0/k_B \ln v$. Uncertainties are comparable to symbol sizes.

ρ_f in the craze. As can be seen, ρ_f is higher for the semi-flexible chains, which have a smaller value of $N_e \approx 30$. Remarkably, we find that λ is a function of N_e only and decreases with decreasing N_e. For instance, while increasing T and r_c produces dramatic coarsening of the fibril structure in Fig. 6 relative to Fig. 4, λ is unchanged. We obtain values of $\lambda_{fl} = 6.0 \pm 0.6$ and $\lambda_{sfl} = 3.5 \pm 0.3$ independent of N, T, and adhesive interaction strength.

In order to understand the dependence of the macroscopic quantity λ on N_e, we analyze the structural changes in the polymer glass during deformation on a microscopic level (see also ref. [10]). Figure 11(a) shows the average final position of beads in the completely evolved craze as a function of their initial positions along the direction of the expansion (z-axis). The average was taken over all beads with initial heights in a bin of width 1a. Although the strain rate is strongly localized during the craze process, the ultimate displacement profile is linear, $z_f = \lambda z_i$.

To measure deviations from a purely affine (uniform) deformation, we evaluated the rms variation δz in z_f for beads in each bin. This quantity is indicated by error bars in Fig. 11(a). Note that the variation in each bin is
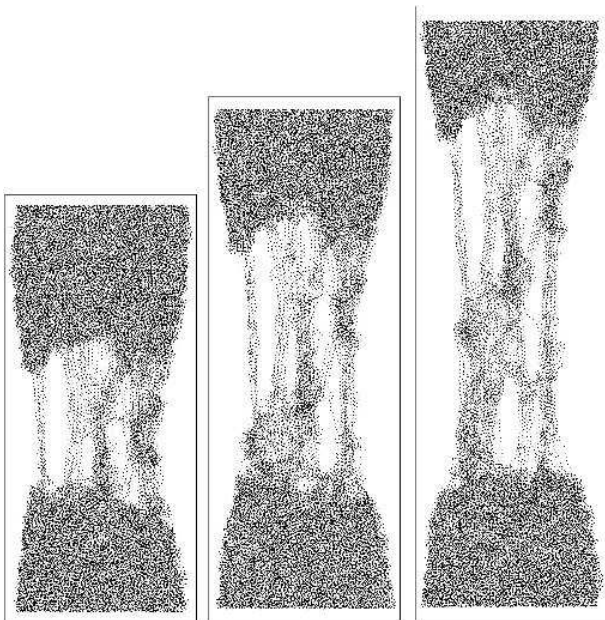
FIG. 11: (a) Final bead heights z_f as a function of initial heights z_i for flexible (large slope) and semiflexible (small slope) chains ($T = 0.1\,\epsilon/k_B$, $r_c = 1.5\,a$). Averages were calculated over z-intervals of width a. Straight lines have slope $\lambda = 5.9$ and $\lambda = 3.5$, respectively. Error bars represent a standard deviation from the averages in each layer and are on the order of $19a$ (flexible) and $9a$ (semiflexible). (b) Square of the height change Δz as a function of the number of covalent bonds ΔN between a bead and the chain center. Dashed straight lines have slope $\lambda^2 l_p l_0/3$ with λ from (a). Deviations from the RW scaling occur in the vicinity of the chain ends (not shown). Other systems at different T, r_c and N show the same results.

FIG. 9: Cross-sections through a craze with a free interface at $T = 0.1\,u_0/k_B$, $r_c = 1.5\,a$, and 262144 beads. Periodic boundary conditions were maintained in the direction into the plane. The location of initial cavitation was constrained by placing repulsive beads in the center plane at $z = L_z/2$. The lateral dimension is $47\,a$ and the vertical dimension is to scale.
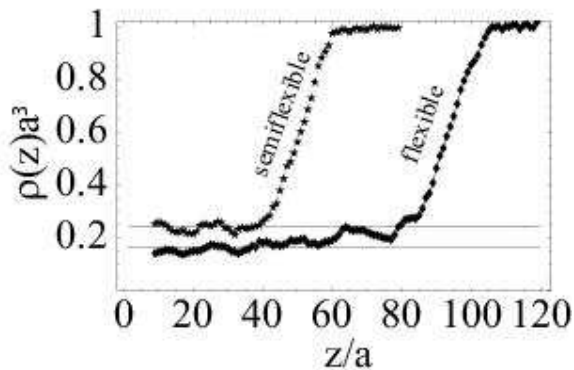

FIG. 10: Density profile through the active zone for crazes with flexible chains ($N_e \approx 70$) and semiflexible chains ($N_e \approx 30$). Horizontal lines indicate the average density in the craze for the two cases.

very reproducible. We find that δz is nearly independent of T and r_c and has values on the order of $19a$ and $9a$ for flexible and semiflexible chains, respectively.

Since no strain is applied in the perpendicular x and y directions, one would assume that there is on average no displacement in these directions. That this is indeed the case is shown in Fig. 12, which repeats the analysis of Fig. 11 for the x-direction. Average final bead positions are identical to initial positions, but there are lateral vari-
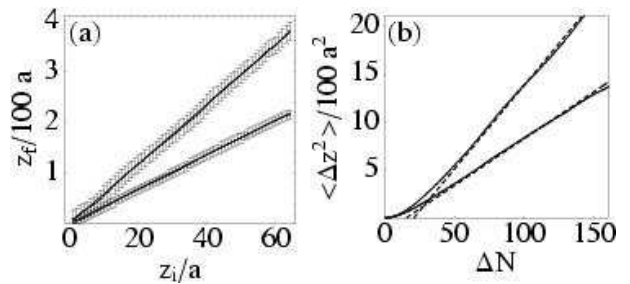
ations δx that are indicated by error bars. These lateral displacements allow chains to gather in fibrils at the initial density to minimize surface area. Unlike the vertical displacements δz, these lateral displacements depend strongly on T and r_c. For example, $\delta x \sim 2.5a$ for the fine structure shown in Fig. 4, where many thin fibrils can be seen, while $\delta x \sim 5.6a$ for the much coarser structure of Fig. 6. In general, δx correlates with the spacing between fibrils as discussed in Section VI and is less than d_i. Krupenkin and Fredrickson [7] suggested that d_i provides an upper bound for the lateral chain deformations.

We now examine changes in the conformation of individual chains. In the initial state, the polymer chains exhibit an ideal random walk (RW) structure inherited from the melt. The average end-to-end vector $\langle \mathbf{R^2} \rangle$ thus scales with the number of covalent bonds connecting two beads ΔN as $\langle \mathbf{R}^2 \rangle = l_p l_0 \Delta N$. The component along each direction is $1/3$ of that value since the initial state is isotropic. Fig. 12(b) shows this initial scaling behavior for $\langle \Delta x^2 \rangle$ (dashed line) and that $\langle \Delta x^2 \rangle$ is not affected by crazing (solid line).

After an affine deformation by λ along z, one would have an anisotropic RW with no change in Δx or Δy, but $\langle \Delta z^2 \rangle = \lambda^2 l_p l_0 \Delta N/3$. Fig. 11(b) shows the actual behavior (solid lines) of $\langle \Delta z^2 \rangle$ in the craze. At large scales, it exhibits the expected scaling for an affine deformation (dashed lines). However, the separation between beads is fixed by the length of the covalent bonds, so the deformation of individual polymers along z cannot be purely affine. At small scales, the linear scaling behavior of $\langle \Delta z^2 \rangle$ crosses over into a quadratic behavior, which indicates that the polymer has been pulled taut on this scale. The typical number of beads in such a straight segment $\tilde{N}_{\rm st}$ can be calculated by let-
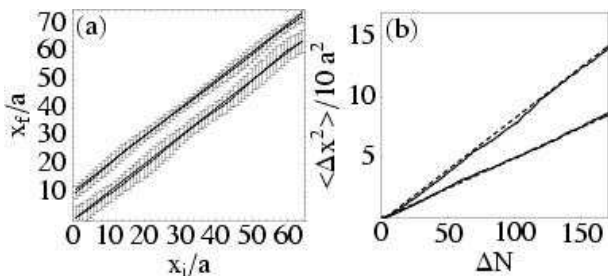
FIG. 12: Analysis of bead positions analogous to the previous figure (same systems), but for the x-positions. No strain is applied in this direction, and the straight lines in panel (a) have slope one. The curves for the semiflexible chains in (a) were displaced vertically upward by 10a to avoid overlap. Error bars represent a standard deviation δx from the averages, and are on the order of 3.7a (flexible) and 2.2a (semiflexible). (b) Bead displacements as a function of distance from the center in bond lengths, ΔN, along the chain. Dashed lines have slope $l_p l_0 / 3$.

ting $(\tilde{N}_{st} l_0)^2 = \langle \Delta z^2 \rangle = \lambda^2 l_p l_0 N_{st}/3$ at the crossover point, which yields $\tilde{N}_{st} = \lambda^2 l_p / 3 l_0$. Inserting the observed values of λ, l_p, and l_0, we arrive at $\tilde{N}_{st}^{fl} = 21 \pm 4$ and $\tilde{N}_{st}^{sfl} = 12 \pm 2$, respectively. These values are comparable to the values of δz found in Fig. 11(a). On this scale, the deformation is non-affine.

The length of taut sections can also be determined by direct analysis of the chain geometry. To this end, we calculate the angle between every covalent bond and the z-axis and label a bond as pointing up (down) if the angle is within 45° of the z (-z) axis. We then count the number N_{st} of consecutive up (down) steps. The probability $P(N_{st})$ of finding a straight segment containing N_{st} steps is shown in Fig. 13(a). For both flexible and semiflexible chains, the distribution develops an exponential tail. Like λ, this tail is independent of N, T, and r_c. The characteristic length scales that arise from these tails are $\tilde{N}_{st}^{fl} \sim 21$ and $\tilde{N}_{st}^{sfl} \sim 13$, in good agreement with the prediction from the RW argument. Fig. 13(b) shows that very similar length scales arise from an equivalent analysis of the decay of the correlation function for the z-component of successive bonds.

In section II B 1, we introduced the standard scaling argument Eq. (2) that relates extension ratio and entanglement length, which has been verified experimentally with great success. In our cases, it predicts $\lambda_{max}^{fl} = 6.5$ and $\lambda_{max}^{sfl} = 3.5$, which agree with the observed values of λ. However, the argument was motivated by the idea that segments between entanglements become fully stretched and thus appears to be at odds with the finding of an average straight segment length of only $N_e/3$ rather than N_e. This discrepancy is resolved by realizing that since the deformation is uniaxial, only the projection of d_i onto the z-axis, $d_i \cos(\Theta_z)$, is expanded, where Θ_z is the angle between d_i and the z-axis. The *average* projection is thus only $1/\sqrt{3}$ of the total length. Indeed, it was
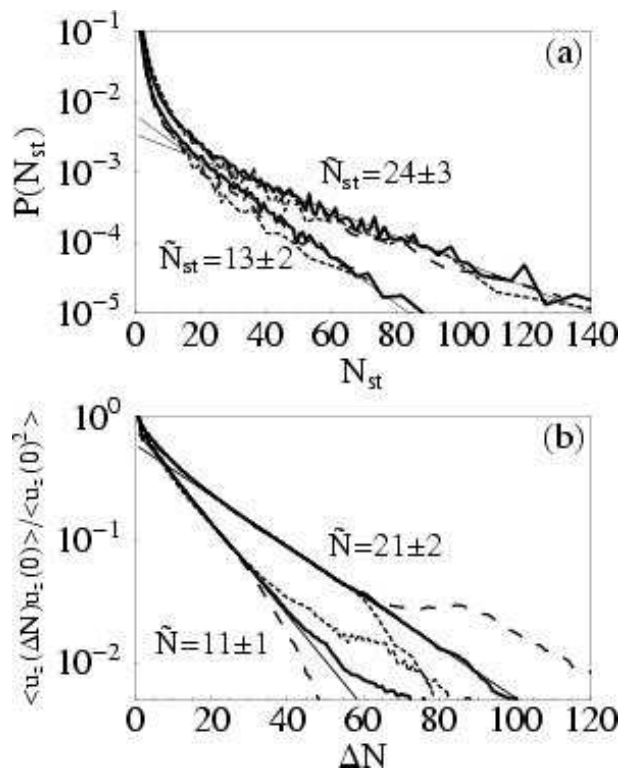

FIG. 13: (a) Probability distribution of straight segments of length N_{st} for flexible and semiflexible chains. Thick lines correspond to simulations at $T = 0.1\,\epsilon/k_B$, $r_c = 1.5\sigma$, $N = 512$ with 1048576 beads. Dotted lines were obtained at $T = 0.3\,\epsilon/k_B$, $r_c = 2.2\sigma$, $N = 512$ with 262144 beads, and long dashed lines correspond to $T = 0.1\,\epsilon/k_B$, $r_c = 1.5\sigma$, $N = 256$ with 262144 beads. The straight lines show fits to $\exp(-N_{st}/\tilde{N}_{st}^{(s)fl})$. (b) z-component of the bond-bond correlation function for the same systems. Thin solid lines show exponential fits with the indicated decay lengths.

noted already in earlier work [14] that, due to this geometric factor, λ should be $\sqrt{3}\lambda_{max}$ for fully stretched chains. However, this result is little cited since $\lambda \approx \lambda_{max}$ in many systems and, until our work, there was no reason to expect the length of straight segments to be $N_e/3$.

The emergence of the length scale $N_e/3$ is a consequence of the random nature of the entanglement mesh. Clearly, all strands would be expanded simultaneously by the same factor in a regular mesh as reported in a simulation study by Stevens [27]. By contrast, in the polymer glass only the segments that are initially aligned with the stretching direction become fully stretched. These fully stretched segments are able to prevent further extension, because the entanglements act like chemical crosslinks. Barsky and Robbins have confirmed the equivalence between entanglements and crosslinks by adding permanent crosslinks randomly to the system [37]. The length between constraints then decreases from N_e, and λ_{max} decreases accordingly. They found $\lambda \approx \lambda_{max}$ in all cases and that the *average* stretched length N_{st} remains at $1/3$

TABLE I: Dissipation during craze growth and covalent contribution to the crazing stress S for several different systems of size 262144.

	T	r_c	N	$\delta Q/\delta W$	% cov stress
fl.	0.1	1.5	256	0.88	87
fl.	0.1	1.5	512	0.88	88
sfl.	0.1	1.5	256	0.71	95
sfl.	0.1	1.5	512	0.67	97
fl.	0.1	2.2	512	0.92	69
sfl.	0.1	2.2	512	0.71	75
fl.	0.3	2.2	512	0.87	61
sfl.	0.3	2.2	512	0.78	67

of the distance between constraints.

The success of the scaling argument Eq. (2) and the constancy of the extension ratio imply that there is no appreciable loss of entanglements in our simulations during craze growth. Chains do not disentangle once $N > 2N_e$, and chain scission (see also section VII) is not observed during growth for any choice of parameters in our model.

E. Energy dissipation and stress transfer during crazing

The work done in transforming a volume dV of polymer into a craze is $\delta W = S(\lambda - 1)dV$. This work can either increase the potential energy dU or be dissipated as heat δQ. The division between energy and heat is hard to determine experimentally, but simulations with short chains found that both contributions were substantial [8]. We have measured δW and the energy change directly in our simulations and calculated δQ using the first law of thermodynamics: $\delta Q = dU - \delta W$. dU can be calculated directly from the bead positions and interaction potentials. Table I shows the fraction $\delta Q/\delta W$ of dissipated total work for a number of large systems. In all cases, a large percentage, $\sim 80\%$, of the total work is dissipated, and only $\sim 20\%$ is stored as potential energy. Since the craze drawing stress varies logarithmically with velocity (see Fig. 8(b)), these percentages could change with velocity. However, we find that dU also decreases with decreasing velocity, and there is no measurable change in the percentage of work converted to heat over at least two orders of magnitude in velocity.

Stress in the craze can also be partitioned into two components that originate either from van der Waals (LJ) interactions Eq. (6) or from covalent interactions Eq. (7). The two contributions are very different in the uncrazed and crazed material. In the undeformed polymer, the tensile stress is mainly carried by the vdW bonds. This stress is transferred in large part to the covalent bonds as they pass through the active zone. Evidence for this is provided in Fig. 14, which shows the covalent and LJ contributions to the total stress as a function of height in the widening direction. Panel
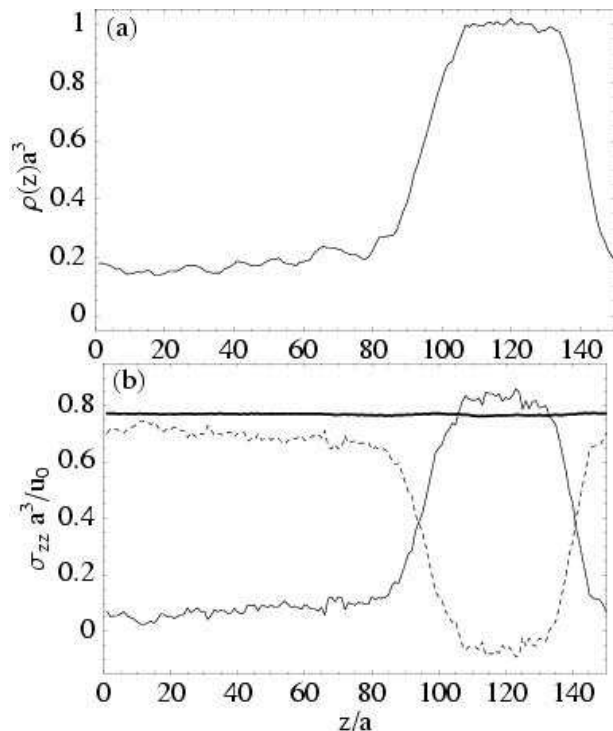

FIG. 14: (a) Density profile through a craze simulation at $T = 0.1u_0/k_B$, $r_c = 1.5a$ with flexible chains. (b) vdW stress (solid line), covalent stress (dashed line) and total stress S (thick line) as a function of position along z. The kinetic contribution to the stress is split evenly between the covalent and vdW stress here and in Table I.

(a) displays the density profile in order to identify dense polymer regions (high density) and craze regions (low density). In Panel (b) one observes that in the dense region all the tension is carried by the van der Waals bonds and the covalent bonds are under slight compression. In the craze, between $60 - 95\%$ of the total stress (see Table I) is carried by the covalent bonds, and the van der Waals bonds only contribute a small fraction.

F. Problems with the capillary models

The results presented so far reveal serious difficulties with the surface tension models discussed in the Introduction. The first evidence of this comes from the observation that S is independent of system size. In our smallest simulations of lateral width $32a$ the simulation box only contains a few fibrils at $T = 0.1u_0/k_B$, $r_c = 2.2a$. If S were controlled by Eq. (4), one should expect that the simulation box would need to contain a statistically significant number of fibrils of spacing $\langle D_0 \rangle$ for S to reach its steady state value. However, the value of S does not fluctuate as the lateral dimensions are increased to $64a$ or $128a$.

The second and more severe problem concerns the dis-

tribution of stress in the craze. The surface tension model assumes that *all* the stress is carried at the interfaces of fibrils or in viscous stress in the active zone. However, Table I and Fig. 14 show that almost all the stress in the fibrils is carried by the covalent bonds, while the surface tension is entirely associated with broken vdW bonds and small entropic contributions.

In the following, we make an alternative proposition to relate craze microstructure and drawing stress. This proposition is based on the observation that the values of S and λ obtained from our simulations obey the equality

$$S_{\mathrm{fl}}\lambda_{\mathrm{fl}} = S_{\mathrm{sfl}}\lambda_{\mathrm{sfl}} = S_0(T, r_c, v). \tag{12}$$

This can be verified for each T and r_c using $\lambda_{\mathrm{fl}} = 6.0$, $\lambda_{\mathrm{sfl}} = 3.6$ and values of S from Fig. 8. Since the fraction of area occupied by the fibrils is $1/\lambda$, S_0 is the local stress within the fibrils.

It is perhaps surprising that the value of local stress needed to draw fibrils is independent of the entanglement length. In order to further test Eq. (12), it would be desirable to consider additional values of N_e and thus λ. Unfortunately, reliable values for N_e exist for only a few values of b. It is, however, not necessary to know N_e for the present purpose, since both S and λ can be measured directly from the craze simulation. Moreover the entanglement length should only depend upon the chain statistics [36], and glassy states with arbitrary statistics can easily be created. We confirmed that simulations with the same persistence length in the undeformed glass gave the same values of λ and S independent of whether the bond-bending potential (Eq. (8)) was included. Fig. 15(a) compares stress strain curves for $b = 0u_0$ at four values of the initial persistence length. Increasing l_p lowers λ and increases S. However, Fig. 15(b) shows that all curves can be collapsed if σ_{zz} is scaled by λ and the extension by $\lambda - 1$. This confirms that S_0 is the stress that controls craze growth and only depends on the van der Waals interactions. An experimental version of this test would be difficult, since it is hard to change N_e for real polymers without changing the chemistry as well.

It is interesting to compare values of S_0 to the stresses required for shear yielding and cavitation, which are also independent of chain statistics. Table II compares these three stresses for two ranges of the LJ potential. Here $b = 0u_0$, but the bond-bending potential has little effect on the values. The three stresses are clearly correlated, decreasing with increasing temperature and decreasing r_c. The local fibril stress is always about twice the cavitation stress and ranges from 7 to 12 times τ_0. The implication is that local stress for drawing material into fibrils S_0 is related to the bulk yield stresses, but it is difficult to determine the relative role of shear and cavity growth. It is interesting to note that the experimental values of S_0/τ_0 for PS and PMMA are about 5 [14, 40], and it would be useful to have values of this ratio for other polymers. A comparison to p_{cav} would also be in-
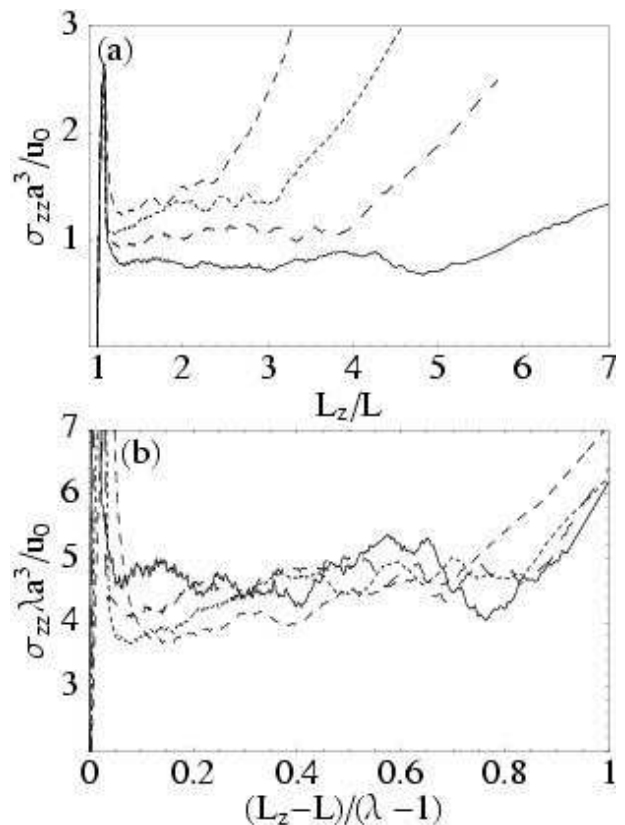

FIG. 15: (a) Stress-strain curves for crazes with $l_p = 1.65a$, $2.2a$, $2.7a$, and $3.3a$ in order of increasing height at $T = 0.1u_0/k_B$, $r_c = 1.5a$ and $b = 0u_0$. The corresponding values of λ are given in Table III. (b) Rescaling of the same data in the form $\sigma_{zz}\lambda$ versus $(L_z/L - 1)/(\lambda - 1)$. All curves collapse onto a common plateau $S_0 = S\lambda \approx 4.5u_0/k_B$ of the same length.

TABLE II: Values of the shear yield stress τ_0, the yield stress for cavitation p_{cav} and the local fibril stress S_0 as a function of temperature. Stresses are in units of u_0/a^3. Uncertainties are ± 0.02 in τ_0, and about 10% in the other quantities.

	$r_c = 1.5a$			$r_c = 2.2a$		
Tk_B/u_0	0.3	0.1	0.01	0.3	0.1	0.01
τ_0	0.23	0.49	0.72	0.45	0.64	0.83
p_{cav}	1.2	2.7	3.0	3.0	4.8	5.0
S_0	2.9	4.5	5.2	5.9	8.0	—

teresting, but its value is sensitive to system size, strain rate and inhomogeneities and it is difficult to measure experimentally.

Given that previous results for N_e [25, 26, 29] are consistent with values inferred from the extension ratio (Eq. 2), our results for λ as a function of l_p allow a rapid estimation of N_e. Table III presents results for a wide range of l_p and shows that the product $N_e l_p$ is constant within our errorbars. Fetters *et al.* [36] have presented a model for the relation between chain statistics and N_e

TABLE III: Measured values of λ, with uncertainties, as a function of l_p and the corresponding range of values of N_e and $l_p N_e$ inferred from Eq. 2. Runs were made at $T = 0.1 u_0/k_B$, $r_c = 1.5a$ and $b = 0u_0$.

l_p	λ	N_e	$l_p N_e$
1.65	6.0 ± 0.6	50-76	83-124
2.2	4.5 ± 0.5	37-57	81-127
2.7	3.5 ± 0.3	29-41	78-111
3.3	3.0 ± 0.3	25-37	83-122
5.55	2.0 ± 0.2	19-28	105-155

that predicts

$$N_e \propto \frac{N^3}{\langle R^2 \rangle^3} \qquad (13)$$

where $\langle R^2 \rangle = l_p l_0 N$ denotes the average end-to-end vector of the polymer chain and the proportionality constant only depends upon density. This implies $N_e \propto l_p^{-3}$, while our data is clearly consistent with a simple inverse relation $N_e \propto l_p^{-1}$. Equation (13) describes many experimental polymers, but it is difficult to change l_p without changing all the other parameters in the equation. The flexible model ($b = 0u_0$) is known to be quantitatively inconsistent with Equation (13) [25], which has been one motivation for studies of more rigid models. It would be interesting to have additional values of l_p from melt simulations to test whether the inverse relation between N_e and l_p found here holds more generally, and, if so, to understand its origin.

G. Width of the active zone

At the interface between dense polymer and craze, polymer chains are locally mobilized and brought into the new fibril structure. The region in which this motion takes place is called the 'active zone'. In Fig. 2 the height of the active zone h was defined as the distance between undeformed polymer layer and the void ceiling, and this layer was assumed to behave like a strain-softened fluid. The main drop in density should occur over the height of the void ceiling of order $\sim \langle D_0 \rangle/2$ [15]. In this section, we compare this simple picture to our simulations.

Fig. 10 shows typical results for the density profile near the craze boundary. For both flexible and semiflexible polymers, the density drops over a region of width $\sim 20a$. The average strain rate $\dot{\epsilon}$ must be localized in the same region, since $\dot{\epsilon} = -\partial \ln \rho / \partial t$. If the active zone advances at velocity v then $\dot{\epsilon} = \pm v \partial \ln \rho / \partial z$ (the sign depends on whether the top or bottom interface is growing). In Fig. 16(a) we present $\dot{\epsilon}$ as a function of position along z. Averages were taken over layers of height $1a$. The curves shown correspond to the 4 different values of l_p used in the creation of the polymer chains. As discussed above, this varies the entanglement length N_e. Curves were shifted by z_0, which corresponds to the center of the peak. At this point, the density is roughly halfway
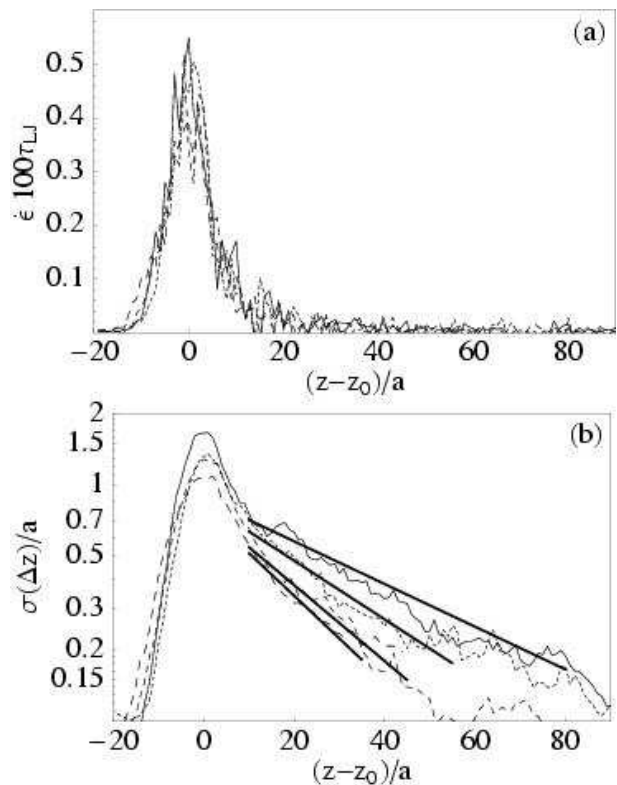

FIG. 16: (a) Strain rate $\dot{\epsilon}$ as a function of distance from the location of the onset of density drop z_0 for 4 values of N_e (see text). Positive values of $z - z_0$ measure the distance into the crazed region. The length of the dashes increases with decreasing N_e. (b) Standard deviation $\sigma(\Delta z)$ from the average displacements along z in a given layer over a time interval of $75\,\tau_{\rm L.J.}$. $\sigma(\Delta z)$ decays exponentially into the craze and the straight lines show fits to this decay with characteristic length scales $48a$, $35a$, $27a$, and $24a$.

between ρ_i and ρ_f. Curves for very different N_e essentially overlap with a width of $\sim 10a$ at half maximum and $\sim 20a$ at the base. The latter corresponds to the range of rapid density change in Fig. 10.

The width of the region over which beads are mobilized was determined from the relative diffusion as a function of height. Fig. 16(b) shows the standard deviation of displacements in the lengthening direction $\sigma(\Delta z)$. The curves peak at the same location as the curves in Fig. 16(a), but are more asymmetric. In the direction of the dense polymer glass $\sigma(\Delta z)$ and $epsilon$ fall to zero over a comparable range. By contrast, $\sigma(\Delta z)$ shows a long exponential tail into the craze with a characteristic decay length $l_{\rm AZ}$ that varies with entanglement length. The fit values of $l_{\rm AZ}$ indicate that there is a definite trend to larger values as N_e increases, and $l_{\rm AZ}$ tends to be somewhat smaller than N_e. This result is not surprising, because N_e is the longest length scale over which particle mobilization should occur. Standard deviations of the lateral displacements Δx and Δy are smaller, but show essentially the same decay lengths.

The above analysis indicates that while the mobility of the beads is constrained by entanglements, the regions of localization of strain rate and the density drop are related to the craze microstructure (see Section VI) . Typical values for $\langle D \rangle$ and $\langle D_0 \rangle$ are given in Table IV. From this, $\langle D_0 \rangle / 2 \sim 10a$, which compares well to the width of the strain localization peak at half maximum. Experimentally, the width of the active zone has been measured by a gold decoration technique [15]. It was concluded that it lies between $\langle D \rangle$ and $\langle D_0 \rangle$, which agrees with our results.

VI. MICROSTRUCTURE OF CRAZES

Another fascinating aspect of crazes is their complicated microstructure. Figs. 4 - 6 give an impression of the range of length scales appearing in the voided fibril network. Clearly, the picture of cylindrical fibers and void fingers (Fig. 2) is an oversimplification. It is nevertheless helpful to build more realistic models starting from this simple scenario.

A. Structure factor

Experimentally, the standard measurement of the craze microstructure is done via scattering experiments. The scattering intensity in these measurements is proportional to the structure factor

$$S(\mathbf{k}) = \frac{1}{N} \left\langle \sum_{j,k} e^{-i\mathbf{k}(\mathbf{r}_j - \mathbf{r}_k)} \right\rangle \qquad (14)$$

times the form factor for the monomers. Since the craze structure has azimuthal symmetry, one decomposes the wavevector $\mathbf{k}$ into components parallel and perpendicular to the fibrils. Contour plots of $S(k_\perp, k_\parallel)$ for two crazes are shown in Fig 17. The microstructure was varied by changing the cutoff length r_c and chain flexibility. Both patterns are asymmetric with the intensity decaying much faster in the direction parallel to the fibrils than perpendicular to them.

Most experimental setups integrate over $k_\parallel$ using slit collimation and measure the integrated structure factor $S(k_\perp) = \int_\infty dk_\parallel S(\mathbf{k})$. In Fig. 18(a), we plot $S(k_\perp)$ as a function of the magnitude of $k_\perp$ for the same systems shown in Fig. 17. At large wavevectors, the curves rise to a peak at $\sim 2\pi/a$ (not shown), which corresponds to the typical separation of two beads. This length scale is so short that it is usually not resolved in typical experimental scattering plots shown in e. g. [21]. The characteristic feature of $S(k_\perp)$ is found at smaller $k_\perp$ in form of a power-law regime with exponent -3. The extent of this scaling regime is bound at large wavevectors by the small scale cutoff provided by the interparticle spacing and at small wavevectors by the distance to the next fibril. The power-law regime is more pronounced for the
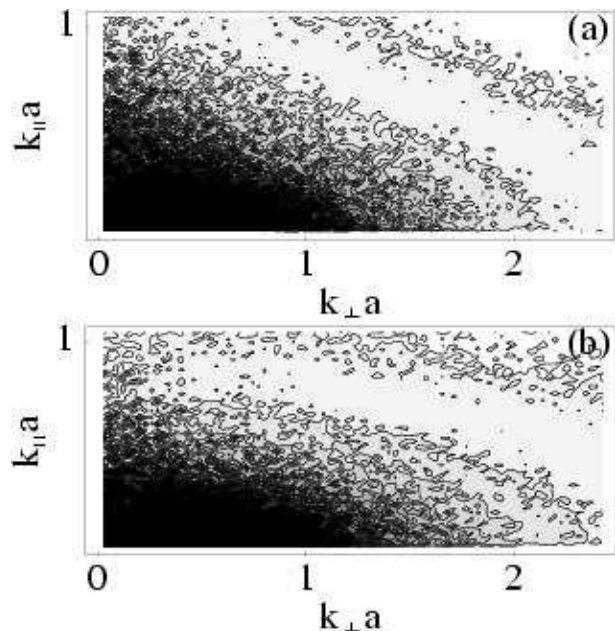

FIG. 17: Contour plots of the structure factor of crazes with (a) flexible chains, $r_c = 1.5a$ and (b) semiflexible chains, $r_c = 2.2a$. The temperature was $T = 0.1u_0/k_B$ and the systems contained 1048576 beads. Colors range from black (high intensity) to white (low intensity).

crazes shown in Fig. 18(b), which were created at higher temperatures where $\langle D_0 \rangle$ is bigger.

B. Interpretation of scattering data

The traditional interpretation of craze scattering data begins with idealizing a craze fibril as a straight cylinder of diameter D and length l along z. The scattering intensity is then proportional to the squared magnitude of the form factor for such a cylinder [21],

$$F(k_\perp) = \frac{\Delta\rho_{el}\pi D^2 l^{1/2}}{2} \frac{J_1(\pi D k_\perp)}{\pi D k_\perp}, \qquad (15)$$

where $\Delta\rho_{el}$ denotes the electron density and J_1 is the first-order Bessel function. Due to the asymptotic behavior of $J_1(x) = (2/\pi x)^{1/2} \cos[x - 3\pi/4] + \mathcal{O}(x^{-1})$ for large arguments, the scattering intensity of a single cylinder will exhibit an oscillating power-law behavior, $|F(k_\perp)|^2 \propto k_\perp^{-3}$. This is also called *Porod* scattering.

In general the fibrils do not have a single diameter, but rather a diameter distribution $P(D)$. One can introduce an average scattering intensity

$$I_0(k_\perp) = \langle F(k_\perp)^2 \rangle = \int_{D_{\min}}^{D_{\max}} dD P(D) F(k_\perp)^2. \qquad (16)$$

by averaging the form factor over the diameter distribution and neglecting correlations between fibrils. The

FIG. 19: Typical crosssection through a craze from flexible chains, $r_c = 1.5\,a$, $T = 0.1\,u_0/k_B$. The lateral dimension is $128\,a$. Fibrils appears as clusters of varying size, and the distributions in Fig. 20 are calculated form these crosssections (see text).
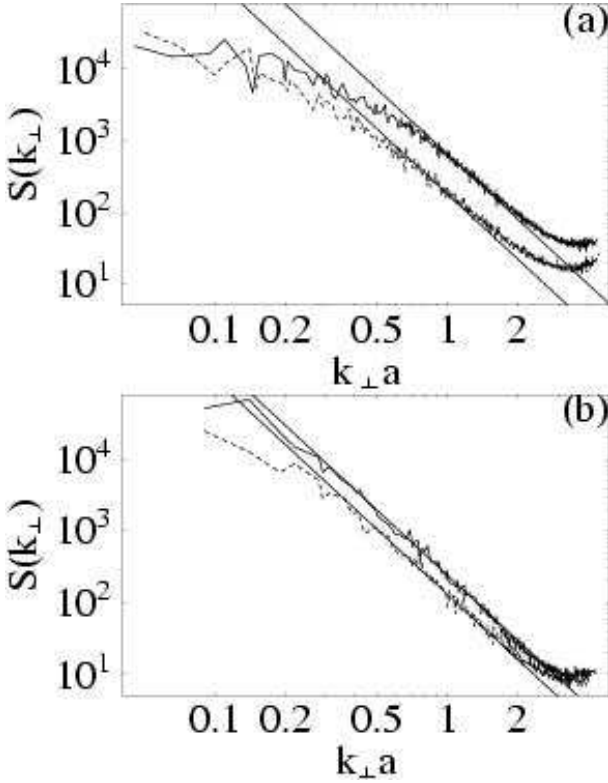
FIG. 18: Integrated structure factor of crazes (a) at $T = 0.1u_0/k_B$, flexible chains, $r_c = 1.5a$ (solid) and semiflexible $r_c = 2.2a$ (dashed) and (b) at $T = 0.3u_0/k_B$, flexible (solid) and semiflexible (dashed) chains with $r_c = 2.2a$. The straight lines have slope -3. System sizes were 1048576 beads in (a) and 262144 beads in (b).

main effect is to smooth out the oscillations so that a straight power-law tail results. The average diameter $\langle D \rangle = \int D P(D) dD$ can be obtained via a Porod analysis, in which one determines the prefactor α to the power-law tail, $S(k_\perp) = \alpha k_\perp^{-3}$. This can be related to $\langle D \rangle$ [19, 20] through,

$$\langle D \rangle = \frac{Q}{\pi^3(1 - 1/\lambda)\alpha}, \quad (17)$$

where $Q = \int dk_\perp 2\pi k_\perp S(k_\perp)$ is a scattering invariant. Values for $\langle D \rangle$ obtained from this formula are collected in Table IV.

The craze fibrils do not all have the same distance from each other, but have in general varying distances that can be described by a radial distribution function $g(r)$. This will lead to interference effects in the scattering intensity that can be described by an interference function $j(k_\perp) = I(k_\perp)/I_0(k_\perp) - 1$. The interference function is related to $g(r)$ by [21]

$$g(r) = 1 + \frac{\pi\langle D \rangle^2 \lambda}{4} \int_0^\infty 2\pi k_\perp j(k_\perp) J_0(2\pi r k_\perp) dk_\perp. \quad (18)$$

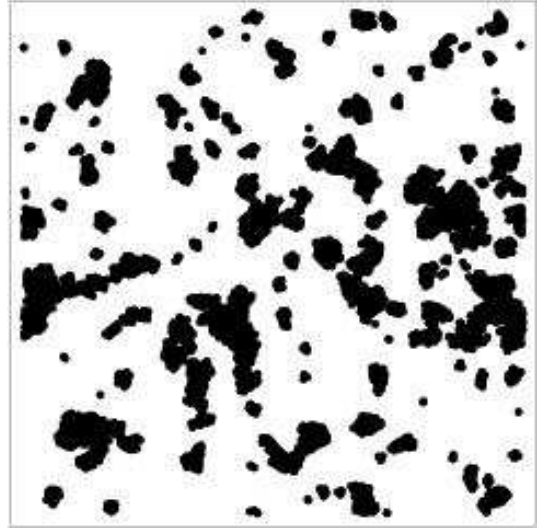As a result, the power-law tail will be modified at small

wavevectors. In particular, the first peak in $g(r)$, corresponding to a typical fibril separation $\langle D_0 \rangle$, should translate into a maximum in $I(k_\perp)$.

The Porod scattering law $|F(k_\perp)|^2 \propto k_\perp^{-3}$ is well confirmed at higher temperatures in Fig. 18(b), while the power-law regime is shorter at lower temperatures. Visual inspection of the craze images suggests that the straight cylinder approximation is not so well justified in this case. Fibrils branch more often and intersect the z-axis at varying angles. At the higher temperature, the chains are more mobile and can align more easily, but they are still not ideal cylinders. We note furthermore that the curves shown in the log-log plot of Fig. 18 do not exhibit a clear maximum (a maximum would be more easily identifiable in a linear plot normally used for experimental results). This would suggest that the ordering of fibrils is mostly random without a clear characteristic separation. However, our statistics are limited by the system size at these large length scales.

C. Distributions of fibril diameter and spacing from real space analysis

In a previous analysis of scattering data [20] for polystyrene and polycarbonate crazes, Eqs. (15)-(18) were used to extract the diameter distribution $P(D)$ and $g(r)$ by means of a detailed fitting procedure. The craze images shown above suggest that $P(D)$ is rather broad, and wide distributions for $P(D)$ were found for both materials, with a significant increase in breadth for polycarbonate [21].

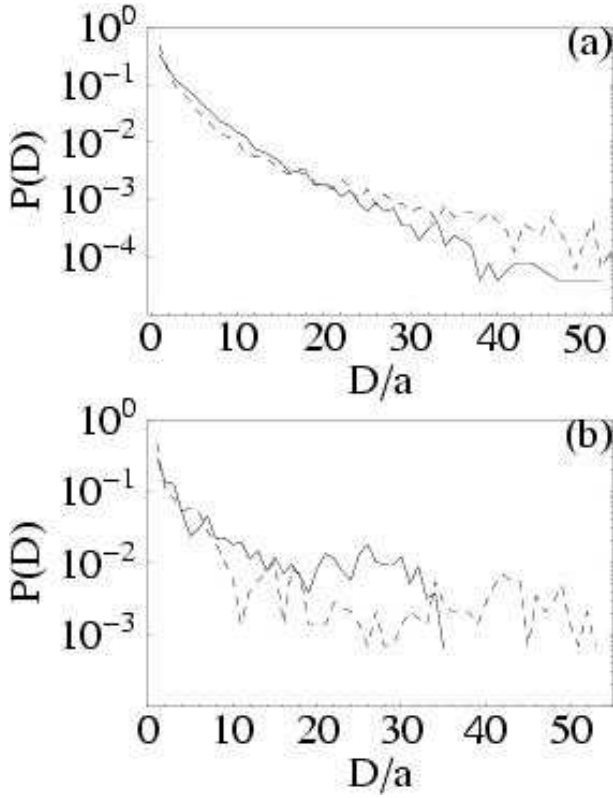Here, we access these distributions by direct geomet-

FIG. 20: Distribution of fibril diameters from analysis of connected clusters (see text) for the same crazes as in Fig. 18(a) and (b). Solid lines refer to flexible chains, dashed lines to semiflexible chains.

TABLE IV: Structural parameters of model crazes. Size refers to the total number of beads in the simulation. For the fibril spacing, results for $\langle D \rangle$ from both the scattering analysis and the cluster analysis (see text) are shown. The rms variation $\sigma(D)/a$ was obtained from cluster analysis.

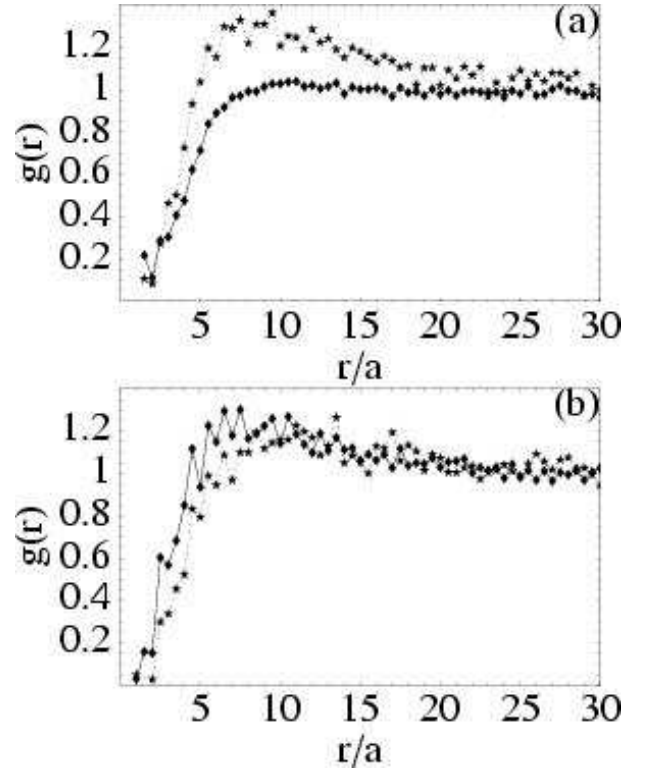| T	r_c	size	$\langle D \rangle/a$ scatt.	$\langle D \rangle/a$ cluster	$\sigma(D)/a$	$\langle D_0 \rangle/a$
sfl.	0.3	1.5	128^3	6.1	5.1	9.4	18.4
sfl.	0.3	2.2	128^3	11.3	6.8	13.1	25.0
fl.	0.1	1.5	64×128^2	4.7	4.2	4.1	14.3
sfl.	0.1	1.5	64×128^2	4.8	4.0	5.5	12.8
fl.	0.1	2.2	64×128^2	8.4	5.5	7.0	22.3
sfl.	0.1	2.2	64×128^2	8.2	5.3	9.5	19.8
fl.	0.3	2.2	64^3	12.6	7.9	8.7	30.7
sfl.	0.3	2.2	64^3	11.1	6.5	10.4	23.5

FIG. 21: Radial distribution function $g(r)$ from analysis of connected clusters (see text). The systems shown are (a): $T = 0.1u_0/k_B$, $r_c = 1.5a$, flexible ($\blacklozenge$) and $r_c = 2.2a$, semiflexible ($\star$), (b): $T = 0.3u_0/k_B$, $r_c = 1.5a$ ($\blacklozenge$) and $r_c = 2.2a$ ($\star$) (both semiflexible).

rical analysis of the bead positions. To this end, we bin the particle positions onto a square grid with gridsize $1a$ normal to the widening direction and take lateral cross-sections of height $1.5a$. As illustrated in Fig. 19, a fibril now appears as a 2-dimensional connected cluster, whose area A is taken to be the sum of the areas of the occupied squares. We define $D = \sqrt{4A/\pi}$.

Fig. 20 shows the resulting distributions of D. As expected, $P(D)$ is very broad. The distributions for flexible and semiflexible chains are very similar at small D for a fixed temperature, but differ for larger D. The tail of the distributions could be fitted to an exponential function, but our statistics are too small for a conclusive statement. Mean values of the diameter are given in Table IV together with the standard deviations of the distributions. The large values of the latter suggest that $\langle D \rangle$ has to be used with care when describing the craze microstructure. Previously, Baljon and Robbins reported similar values of $\langle D \rangle = 7a$, $\sigma(D) = 11a$ for flexible chains at $T = 0.3u_0/k_B$, $r_c = 1.5a$ [9].

The value of $\langle D \rangle$ obtained from the Porod analysis is always larger than the value from the cluster (real-space) analysis. Both values rise with increasing adhesive interaction and increasing temperature as expected. Taking $a \sim 0.8$nm, diameters in our model crazes would corre-

spond to a range of $\langle D \rangle = 1.4 - 6.3$nm, which is at the small end of the experimental range. The reason is that an artificially small value of the surface tension and a high widening velocity v are used here. Both lower $\langle D \rangle$, which allows us to use smaller system sizes.

An estimate for the mean fibril spacing $\langle D_0 \rangle$ can be obtained by equating the area per fibril, $\pi D_0^2/4$, to the inverse areal density $1/n$, i.e. $\langle D_0 \rangle = 2\sqrt{1/n\pi}$. The areal

density was obtained by counting the number of separate fibrils per cross-section. Values for $\langle D_0 \rangle$ are also given in Table IV and translate into a range between 10 nm and 25 nm. The higher numbers are comparable to experiment and are obtained with $r_c = 2.2a$, which produces more realistic surface energies.

In order to obtain the radial distribution function of the fibrils, we continued the analysis described above and calculated the center of mass for each 2D cluster. The positions given by this procedure were used to calculate $g(r)$ in Fig. 21. In general, these functions have very little structure. There is a size exclusion minimum at the origin, and the curves have a weak first maximum around $10a$. As the fibrils become thicker, the location of the maximum shifts to larger values. Qualitatively similar curves were obtained from experiment [21], which confirms the basically random nature of fibril positions. The height of the maximum is too small to be reflected in the scattering intensity.

VII. STRESS DISTRIBUTION AND CRAZE BREAKDOWN

In regime III of the stress-strain curve of Fig. 7 the entire volume of the simulation cell has been converted to a craze. Elongation past the extension ratio causes uniform straining of the craze and eventually leads to craze failure. Studies of this regime are directly relevant to crack propagation in glassy polymers (Fig. 1). The stress in the craze region rises from S at the active zone to a maximum value $S_{\max}$ at the crack tip. The elastic properties of the craze determine the rate at which the stress rises with distance, and $S_{\max}$ determines how large the craze region can become before the crack propagates [5]. These properties were recently obtained from MD simulations and combined with continuum theory to predict the macroscopic fracture energy [6]. Here we focus on the microscopic stress distribution and its relation to $S_{\max}$.

A. Disentanglement versus chain scission

The craze can fail by two different mechanisms that depend on the chain length N: short chains can disentangle, while very long chains fail through chain scission [6]. Both limiting behaviors and the crossover between them can be addressed through our simulations. As can be seen in Fig. 7, short chains of length $N = 128$ form crazes that grow at the constant plateau stress S, but the stress drops monotonically to zero upon straining past λ. For longer chains, the stress σ_{zz} rises to a maximum value $S_{\max}$ that exceeds S.

Values for $S_{\max}$ were systematically obtained as a function of normalized chain length N/N_e from curves such as those shown in Fig. 7. Fig. 22 summarizes the breaking stresses for the craze fibrils normalized by the break-
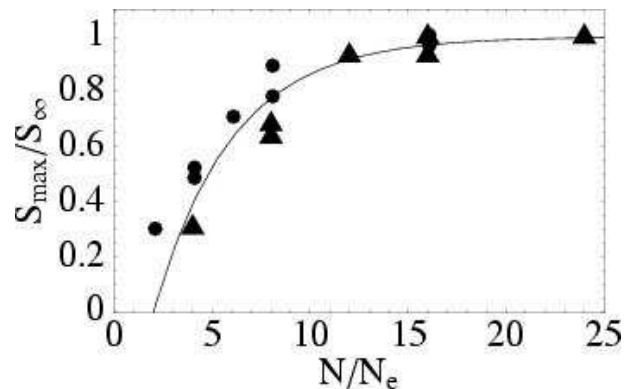

FIG. 22: Saturation of fibril breaking stresses in systems of size 262144 beads, $T = 0.1u_0/k_B$. S_∞ denotes the maximum saturation stress in the limit of very long chains. The solid line is $1 - \exp\left(-N/4N_e + 1/2\right)$. Squares indicate flexible chains ($N_e \simeq 64$) and triangles indicate semiflexible chains ($N_e \simeq 32$).

ing stress in the limit of very long chains S_∞. $S_{\max}$ is zero for $N < 2N_e$, since stable crazes do not form for such short chains. $S_{\max}/S_\infty$ first rises roughly linearly with N/N_e, and then saturates at unity for chain lengths longer than about $10N_e$. The saturation coincides with the observation of significant amounts of chain scission. Interestingly, the data seems to collapse onto a single curve (solid line).

Note that the maxima of the stress-strain curves in Fig. 7 are reached at strains of ~ 6 and ~ 10 for flexible and semiflexible chains, respectively. These values are close to $\sqrt{3}\lambda_{\max}$, which implies that at the breaking point the chains are pulled fully taut between entanglement points. This was confirmed by direct analysis of the craze microstructure.

1. Chain end relaxation

In order to understand the crossover regime and the competition between the two failure mechanisms, it is useful to study the distribution of tension along a given chain. Fig. 23 shows the tension as a function of distance from the chain end at several stages of craze breaking. Since the chain ends are identical, symmetry was used to improve statistics. In the unstrained craze (lowest curves), both flexible and semiflexible systems exhibit a constant stress in the center of the chain, but a relaxation toward the free ends. The characteristic length scales for this relaxation were extracted by fitting an exponential decay to the transition region. The values of the decay lengths $N_{\text{end}}^{\text{fl}} = 21$ and $N_{\text{end}}^{\text{sfl}} = 13$ are comparable to the characteristic length of $N_e/3$ for stretched segments, but are not universal. Stronger adhesive interactions were found to increase $N_{\text{end}}^{\text{(s)fl}}$. Upon straining the craze, the tension in the center of the chains and the val-
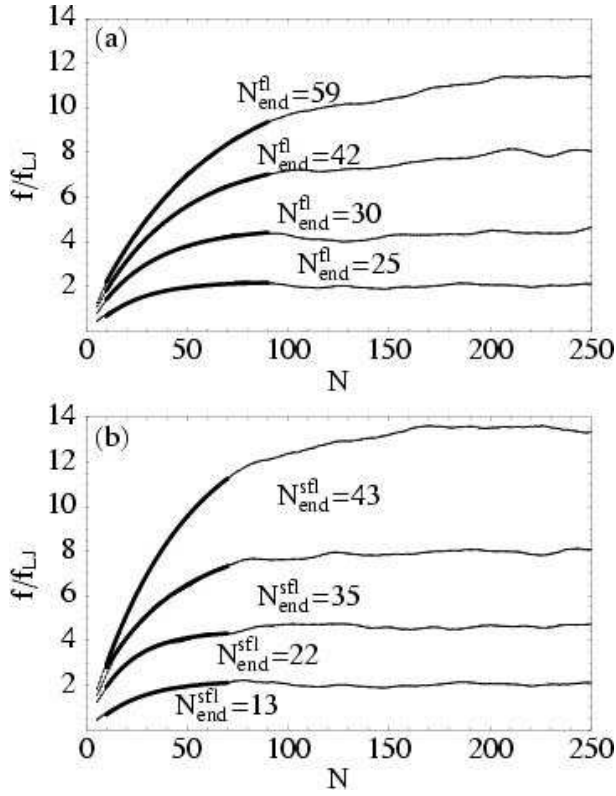
FIG. 23: Distribution of tension along the (a) flexible and (b) semiflexible chains (N=512). The lowest curves corresponds to the unstressed craze and the highest curves show the tension at the breaking point. Two intermediate stages are also shown. The characteristic length scales N_{end} describe the end relaxation and were obtained by fitting the indicated part of the curves to an exponential relaxation.

ues of $N_{end}^{(s)fl}$ rise. At the breaking point (last curves), the end relaxation extends over a length scale comparable to the entanglement length.

These results help to formulate a simple argument for the universal curve plotted in Fig. 22. The *average* distance of an entanglement point from the chain end is $N/4$. We assume that the probability of disentanglement decreases exponentially with distance from the chain end, as suggested by the tension relaxation curves. The characteristic length scale N_{end} at the breaking point in these curves was on the order of N_e. Because of the above, we expect this length scale to be the characteristic decay length for the probability of disentanglement, and thus postulate a disentanglement probability of the form $\exp[-(N - 2Ne)/4N_e]$. Here, N was reduced by $2N_e$, since for this chain length the disentanglement probability is one and the chain is free on either side. The maximum stress can now be written as the limiting value of S_∞ times the probability for non-disentanglement, which gives

$$S_{max}/S_\infty = 1 - \exp[-(N - 2Ne)/4N_e]. \quad (19)$$

Fig. 22 shows that this curve agrees well with the data.

B. Global tension distribution

The parameter governing chain scission and thus the value of S_∞ is the distribution of tension in the polymer craze. In a previous paper [10], we reported that this distribution is characterized by an exponential tail at large tensile forces, in analogy to jammed systems such as granular materials [39]. This distribution is shown in Fig. 24 for flexible and semiflexible chains of length $N = 512$ and several strain states. The tensile (positive) part of the distribution is well fitted by $1/\langle f \rangle \exp[-f/\langle f \rangle]$, where only the positive tensions are included in the average $\langle f \rangle$. Note that $\langle f \rangle$ is the same for flexible and semiflexible chains at the plateau. The distribution with the steepest slope (smallest $\langle f \rangle$) corresponds to the fully developed craze. Additional curves with higher $\langle f \rangle$ correspond to stressed crazes at the same strain with respect to the unstrained craze. Note that the semiflexible and flexible crazes have the same values of $\langle f \rangle$ at each strain. This is related to the fact that the stress S_0 in the fibrils is independent of N_e (see Section V F). The last curve shows the tension distribution at the breaking point where σ_{zz} is largest (see also Fig. 7). The effect of straining the craze only changes $\langle f \rangle$, and all curves could be collapsed after normalizing by $\langle f \rangle$.

We note that in our simulations, no scission or disentanglement occurs during craze growth proper. The fraction of bonds that break at a given average tension is $P_{br}(\langle f \rangle) = \int_{f_c}^{\infty} \exp[-f/\langle f \rangle]df = \exp[-f_c/\langle f \rangle]$. In our simulations $f_c = 100f_{LJ}$ as described in Section III. The onset of scission can be estimated using a simple scaling argument: $N_{bonds}P_{br}(\langle f \rangle) \sim 1$. From this we estimate an average value of the tension at breaking

$$\langle f \rangle = f_c/\ln N_{bonds}. \quad (20)$$

For $N_{bonds} \simeq 262144$, this implies that scission will occur when $\langle f \rangle \simeq 8.0f_{LJ}$, which was confirmed by direct inspection of the chains at the corresponding strains. Such high tensions only occur when the craze is strained past the extension ratio. The largest value of $\langle f \rangle$ observed with the present model during craze growth was $4.5f_{LJ}$ and occurred at very low temperature $T = 0.01u_0/k_B$ and $r_c = 2.2a$.

The degree of chain scission in experimental crazes is still a matter of debate, but it appears likely that at least some chains do experience scission. The absence of scission in the present study is most likely due to the low monomeric friction coefficient of the bead-spring model. As the above argument showed, a relatively modest increase in the average tension will quickly lead to appreciable scission. More realistic polymer models should be able to capture this effect. An increase in system size will likewise raise the number of broken bonds. For a typical value of $\langle f \rangle = 3f_{LJ}$, one bond would break for
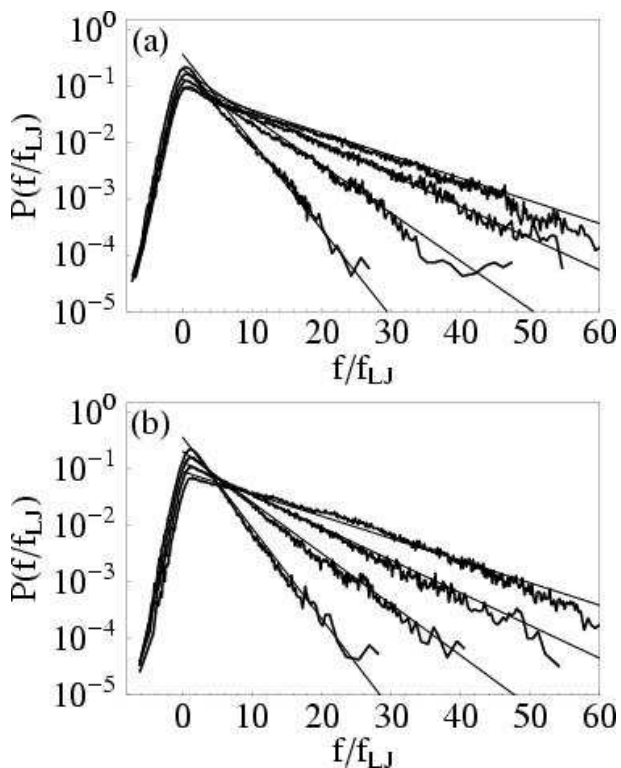
FIG. 24: Distribution of tension in crazes of size 262144 beads with N=512 for (a) flexible and (b) semiflexible chains. Strain states correspond to the ones shown in Fig. 23. The values for $\langle f \rangle$ are $2.9, 4.9, 7.6$, and $11.8 f_{\mathrm{LJ}}$, respectively. $f_{\mathrm{LJ}} = 2.4 u_0/a^3$ is the breaking force of the LJ interaction. The straight lines correspond to $\exp[-f/\langle f \rangle]/\langle f \rangle$.

every 10^{15} bonds. Note that the exponential tension distribution leads to a logarithmic size dependence Eq. (20) and allows for sequential bond breaking. The fibrils are thus much weaker than implied by the common simple assumption that all bonds carry the same tension and break when $\langle f \rangle = f_c$.

VIII. SUMMARY AND CONCLUSIONS

This paper presented molecular dynamics simulations of craze nucleation, widening and breakdown. Initial failure of the LJ polymer glass occurred through shear in biaxial loading. Only when all three principal stresses were tensile did cavitation and craze formation occur. However, once past the nucleation phase, plane stress conditions are sufficient for continuing craze growth. Cavitational failure could be fitted to a cavitation criterion of the form $\tau_{dev}^c = \tau_0^c + \alpha^c p$.

Craze widening proceeds in the simulations by a clearly identifiable fibril drawing process. This interpretation is also well-supported by experiments. The resulting craze microstructure is compellingly similar to TEM images of experimental crazes, and the length scales quantified by

$\langle D \rangle$ and $\langle D_0 \rangle$ are within experimental limits. The simulations clearly establish the connection between extension ratio and entanglement length. In the glass, disentanglement is prevented and the entanglements act like chemical crosslinks. A microscopic analysis of the length of stretched chain segments has shown that unlike the case of a regular mesh, only a few segments are fully expanded to the entanglement length, and the average extension is only $N_e/3$. The factor $1/3$ arises from averaging over all angles that a given segment can form with the stretching direction.

Another salient finding of this study is the exponential distribution of tension in the craze. The presence of large stress fluctuations makes chain scission much more likely than e. g. a Gaussian distribution or uniform loading. Since force distributions of this kind are also often seen in conventional "jammed" systems such as foams, colloids and granular media, we have suggested [10] that a craze can be viewed as a system that jams under tension.

The highly nonequilibrium nature of the force distribution, and the strong concentration of stress in the covalent backbone bonds, formed the basis for our critique of the conventional capillary model of craze widening. The polymer glass is not a viscous fluid in the active zone, and the hydrodynamic description does not apply. The picture suggested by our simulations is that crazing is a form of localized shear deformation, but with a much greater mobilization of material than in standard shear yielding. The very similar rate and temperature dependence of S is another indication of the close relation between the processes. Based on trends observed in the simulations, we have suggested that the local stress in the fibrils $S_0 = S\lambda$ is independent of the entanglement length. S_0 varies with temperature and strength of adhesive interaction in a manner very similar to the yield stresses for shear and cavitation. Establishing a precise connection between these characteristic stresses should be a most interesting direction for future work.

A detailed analysis of the microstructure of crazes was also presented. The calculated structure factor is similar to measured scattering intensities. As in these experiments, a Porod analysis was used to extract a measure of the mean fibril diameter $\langle D \rangle$ from the structure factor. While the extension ratio depends only on N_e, the mean fibril diameter depends on many factors. The value of $\langle D \rangle$ increases with increasing T and with increasing strength of the van der Waals interactions. Chain stiffness has less effect, although $\langle D \rangle$ is larger for flexible chains than semiflexible chains at high temperatures.

The distribution of fibril diameters was determined from the real space structure of the crazes. The average fibril diameter from this method was always smaller than that determined from the structure factor. The distribution was also very wide with a variance that exceeded the mean and a tail extending to many times the mean. The radial distribution function for the fibrils shows almost no correlation, merely an exclusion minimum near the origin. Fibrils merge and split with each other directly,

rather than being joined by smaller cross-tie fibrils.

The simulations described here capture the generic features of experiments on many different polymers and provide previously inaccessible information about the dynamics and microstructure. However, they are unable to address quantitative behavior of specific polymers. Future studies with chemically realistic potentials will be of great value, but require orders of magnitude more computational effort.

IX. ACKNOWLEDGEMENTS

[1] R. N. Haward, R. J. Young, Eds., *The Physics of Glassy Polymers*, (Chapman & Hall, London, 1997).
[2] I. M. Ward, *Mechanical Properties of Solid Polymers* (John Wiley & Sons, New York 1983).
[3] R. P. Wool, *Polymer Interfaces: Structure and Strength*, (Hanser/Gardner, Munich, 1995).
[4] A. V. Pocius, *Adhesion and adhesives technology: an introduction*, (Hanser/Gardner, Munich, 1997).
[5] H. R. Brown, Macromolecules **24**, 2752 (1991)
[6] J. Rottler, S. Barsky and M. O. Robbins, Phys. Rev. Lett. **89**, 148304 (2002).
[7] T. N. Krupenkin and G. H. Fredrickson, Macromolecules **32**, 5029 (1999), Macromolecules **32**, 5036 (1999)
[8] A. R. C. Baljon, M. O. Robbins, Science **271**, 482 (1996).
[9] A. R. C. Baljon, M. O. Robbins, Macromolecules **34**, 4200 (2001).
[10] J. Rottler, M. O. Robbins, Phys. Rev. Lett. **89**, 195501 (2002).
[11] A. S. Argon and M. .M. Salama, Phil. Mag. **36**, 1217 (1977)
[12] A. S. Argon and J. G. Hannoosh, Phil. Mag. **36**, 1195 (1977).
[13] B. D. Lauterwasser, E. J. Kramer, Phil. Mag. **39**, 469 (1979)
[14] E. J. Kramer, Adv. Polymer Science **52/53**,1 (1983).
[15] E. J. Kramer, L. L. Berger, Adv. Polymer Science **91/92**,1 (1990).
[16] C. Creton, E. J. Kramer, H. R. Brown, C.-Y. Hui, Adv. Polymer Science **156**, 55 (2001).
[17] J. Washiyama, C. Creton, E. J. Kramer, Macromolecules **25**, 4751 (1992)
[18] G. H. Michler, Colloid & Polymer Sci. **264**, 522 (1986)
[19] E. Paredes and E. W. Fischer, Makromol. Chem. **180**, 2707-2722 (1979).
[20] H. R. Brown and E. J. Kramer, J. Macromol. Sci. Phys. **B19**, 487 (1981)
[21] H. R. Brown, Mat. Sci. Rep. **2**,315 (1987)
[22] G. J. Salomons, M. A. Singh, T. Bardouille, W. A. Foran, and M. S. Capel, J. Appl. Cryst. **32**, 71 (1999)
[23] G. J. Salomons, M. A. Singh, T. Bardouille, W. A. Foran, and M. S. Capel, Macromolecules **32**, 1264 (1999)
[24] M. Doi and S. F. Edwards, *The Theory of Polymer Dynamics*, (Oxford University Press, Oxford, 1986)
[25] M. Pütz, K. Kremer, G. S. Grest, Europhys. Lett. **49**, 735 (2000).
[26] K. Kremer and G. S. Grest, J. Chem. Phys. **92** 5057 (1990).
[27] M. J. Stevens, Macromolecules **34**, 1411 (2001), Macromolecules **34**, 2710 (2001)
[28] S. W. Sides, G. S. Grest, M. J. Stevens, Phys. Rev. E **64**, 050802 (2001), Macromolecules **35**, 566 (2002).
[29] R. Faller, F. Müller-Plathe, and A. Heuer, Macromolecules **33**, 6602 (2000) and R. Faller and F. Müller-Plathe, ChemPhysChem. **2** , 180 (2001).
[30] M. P. Allen, D. J. Tildesley, *Computer Simulations of Liquids* (Oxford University Press, Oxford 1987).
[31] R. S. Kody and A. J. Lesser, J. Mater. Sci. **32**, 5673 (1997).
[32] R. Raghava, R. M. Cadell, and G. S. Y. Yeh, J. Mater. Sci. **8**, 225 (1973)
[33] J. Rottler and M. O. Robbins, Phys. Rev. E **64**, 051801 (2001).
[34] J. Rottler and M. O. Robbins, in preparation.
[35] T. H. Courtney, Mechanical Behavior of Materials, McGraw-Hill (1990)
[36] L. J. Fetters, D. J. Lohse, D. Richter, T. A. Witten, and A. Zirkel, Macromolecules **27**, 4639 (1994).
[37] S. J. Barsky and M. O. Robbins, in preparation.
[38] H. R. Brown, Macromolecules **24**, 2752 (1990).
[39] A. J. Liu and S. R. Nagel (Eds.), *Jamming and Rheology*, (Taylor & Francis, London, 2001)
[40] R. Quinson, J. Perez, M. Rink, and A. Pavan, J. Mater Sci. **32**, 1317 (1997).
[41] http://www.cs.sandia.gov/~sjplimp/lammps.html.
[42] This is only done in Fig. 9. All other simulations use fully 3D periodic boundary conditions without repulsive beads.